# Permeability evolution during dynamic stressing of dual permeability media

Igor Faoro,[1] Derek Elsworth,[1] and Chris Marone[2]

Received 1 August 2011; revised 23 October 2011; accepted 31 October 2011; published 25 January 2012.

[1] Changes in permeability due to dynamic loading from earthquakes are observed commonly but the underlying mechanisms are poorly understood. This study reports fluid flow-through experiments on fractured rock that reproduce, at laboratory scale, transient changes in permeability that decay to background over extended periods of time. We explore this response as a particular form of poroelastic loading in dual-porosity and dual-permeability media subject to zero net strain but with incremented fracture fluid pressures. Initial augmentation of pore fluid pressure dilates the fracture and compacts the surrounding, low permeability matrix, resulting in a step-like (order of seconds), transient increase in the effective permeability of the rock mass. With time, fluid pressure diffusion into the low permeability matrix then resets the effective permeability to the background magnitude, with the rate controlled by a diffusive timescale. We show that for an increase in fracture pore fluid pressure, the magnitude of the transient increase in fracture permeability scales with the ratios of the pore pressure increase to the intact modulus and the fracture spacing to the initial fracture aperture, for a broad suite of experiments. The duration of the permeability transient, measured via the time to recover background permeability, scales inversely with matrix permeability and modulus of the intact matrix and directly with the square of the spacing between fractures.

**Citation:** Faoro, I., D. Elsworth, and C. Marone (2012), Permeability evolution during dynamic stressing of dual permeability media, *J. Geophys. Res.*, *117*, B01310, doi:10.1029/2011JB008635.

## 1. Introduction

[2] Fluid transmission in fractured rock masses is relevant to a broad variety of scientific and industrial problems and processes (e.g., earthquakes and faulting, exploration for and recovery of geothermal resources, oil production, and groundwater resource development). Although the feedbacks between the transient evolution of permeability and such processes as compaction, hydraulic fracturing, poroelastic response, and dissolution-precipitation reactions have been quantitatively explored [*Connolly*, 1997; *Connolly and Thompson*, 1989; *Dutrow and Norton*, 1995; *Lowell et al.*, 1993, 1995; *Manga et al.*, 2003; *Manga and Brodsky*, 2006; *Muir-Wood and King*, 1993; *Nur and Walder*, 1990; *Rice*, 1992; *Walder and Nur*, 1984; J. Elkhoury et al., Dynamic stress stimulates flow in fractures: Laboratory observations of permeability enhancement, submitted to *Journal of Geophysical Research*, 2011], challenges remain in quantifying rates and even the sense of permeability change in some cases. The mechanisms underlying these responses are poorly understood and thus it is difficult to predict the response to mechanical or chemical perturbations, each of which could lead to changes in fracture face morphology or flow topology. Natural discontinuities such as fractures and cracks are high permeability paths for fluid and mass transport in crystalline rocks. However, as a result of processes related to deformation, dissolution and precipitation of minerals and other diagenetic and metamorphic processes, permeability is a time-dependent property.

[3] Mechanical and chemical compaction of sediments typically results in a gradual evolution of permeability while water-rock interactions, hydraulic fracturing or dynamic and static stressing by earthquakes can cause permeability to evolve more rapidly [*Elkhoury et al.*, 2006; *King et al.*, 1999; *Muir-Wood and King*, 1993; *Quilty and Roeloffs*, 1997; *Roeloffs*, 1996; *Roelofts*, 1998; *Roeloffs et al.*, 1989; *Rojstaczer and Wolf*, 1992; *Rojstaczer et al.*, 1995].

[4] For example, simulations of calcite dissolution in coastal carbonate aquifers suggest significant changes in porosity and permeability over timescales of $10^4$–$10^5$ years [*Sanford and Konikow*, 1989] while analyses of near-surface silica precipitation in hydrothermal up-flow zones indicate that at high temperatures (300°C), large (1 mm) fractures can be sealed by silica precipitation in as little as 10 years [*Lowell et al.*, 1993].

[5] Conversely, the evolution of permeability in fractured aquifers as a result of dynamic stressing by earthquakes occurs rapidly –on timescales associated with the passage of the seismic waves – on the order of 10 s of seconds.

[6] Recent work shows such rapid increases in permeability (*step like permeability changes*), to values many times the

[1]Department of Energy and Mineral Engineering, Center for Geomechanics, Geofluids, and Geohazards, EMS Energy Institute, Pennsylvania State University, University Park, Pennsylvania, USA.
[2]Department of Geosciences, Center for Geomechanics, Geofluids, and Geohazards, EMS Energy Institute, Pennsylvania State University, University Park, Pennsylvania, USA.


0148-0227/12/2011JB008635

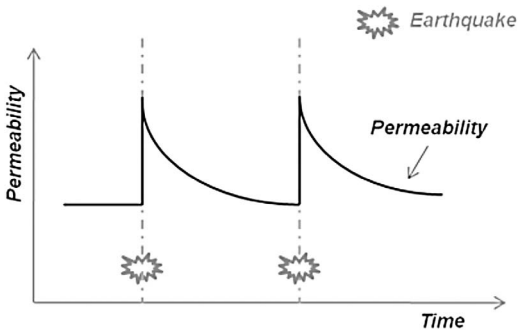


**Figure 1.** Schematic of "step like permeability changes" due to earthquakes.

background [*Elkhoury et al.*, 2006], that decline to background magnitudes over subsequent periods of months to years. A schematic representation of that response is reported in Figure 1.

[7] The purpose of this paper is to explore these enigmatic observations of rapid (order of hours) increase in permeability followed by a slow (order of years) recovery to original permeability recorded in fractured aquifers subject to distant (order of 50 km) earthquakes [*Elkhoury et al.*, 2006]. We examine the effect of poromechanical drainage state on permeability in a fractured, low-permeability rock subject to rapid (undrained) augmentation of fluid pressures and subsequent slow pressure diffusion (drained) into the matrix. We generalize our results for other forms of dynamic stressing.

## 2. Experimental Method

[8] To better understand processes that may contribute to rapid increases of permeability followed by a slow retreat to background magnitudes [e.g., *Elkhoury et al.*, 2006], we examine the role of dynamic stressing through the proxy of fluid pressure augmentation in dual-permeability fractured aggregates. We report laboratory flow-through tests on cores of fractured and unfractured Westerly granite that were uniaxially loaded and subjected to dynamic stressing.

### 2.1. Experimental Setup

[9] The schematic of the experimental set up is represented in Figure 2. Cylindrical samples of Westerly granite (diameter: 44 mm, length: 100 mm), either intact or with tensile fractures perpendicular to the cylinder axis, are uniaxially compressed between two cylindrical platens. In particular the top platen is plumbed with high-pressure fittings for fluid access and connected to a high-precision, servo-controlled pressure intensifier.

[10] Fractures are produced by notching the outer circumference of the sample to a depth of 2 mm and then subjecting the sample to Brazilian-style tensile loading. One half of the sample is then drilled along its major axis, producing a 3-mm diameter borehole. The sample is successively set between the two loading platens once the fracture surfaces have been cleaned with compressed air and re-mated. The inlet fluid (de-ionized water) circulates from the upper platen into an axial borehole that pierces the fracture. Fluid flows from the top of the sample, down the borehole and then radially outward from the center of the fracture, draining at its edge (Figure 2). In order to prevent leakage along the top of the sample, two rubber "*o*" rings (respectively 10 mm and 40 mm in diameter) are used between the top platen and the sample (Figure 2a). Fluid inflow is controlled by a high-precision, servo-controlled pressure intensifier capable of measuring and controlling either flow rate into the sample or fluid pressure.

[11] Axial stress is applied to the sample by a servo-controlled hydraulic ram and measured with a strain gauge load cell accurate to 5 N (3.3 kPa on our sample). As mentioned above, control experiments are also conducted on

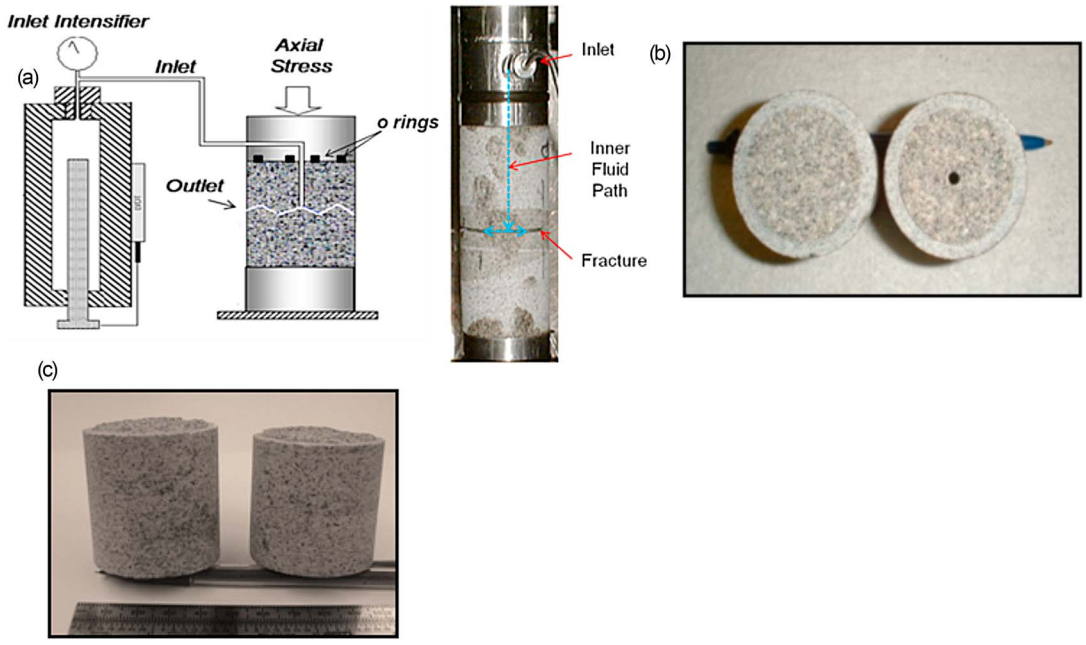


**Figure 2.** Equipment arrangement showing: (a) the experimental design, the tested Westerly core samples, respectively in plan (b) and (c) profile view.

**Table 1.** Variables and Symbols

| Symbol | Name | Parameter Range | Units |
|---|---|---|---|
| $E$ | Young's Modulus | 40–70 | GPa |
| $K_n$ | Fracture Stiffness | 3.3 | GPa |
| $S$ | Fracture Spacing | 100 | mm |
| $\alpha f$ | Biot Coefficient for fracture | 1 | |
| $\alpha s$ | Biot Coefficient for solid matrix | 1 | |

unfractured samples. Table 2 gives details on the full suite of tests.

### 2.2. Experimental Procedure

[12] Flow through experiments are performed at room temperature and began after the samples (fractured and not) were first axially loaded and then locked between the vertical ram and the bottom platen. (The initial total stress values ($\sigma$) are reported in Table 2 and range between 8 to 16 MPa). In this configuration, with the ram locked in place, we independently measure the evolution of axial stress.

[13] We impose a series of step changes in the pore fluid pressure Pp (Table 2) and measured the resulting flow rate via the displacement of the piston within the pressure intensifier, using a *Direct-Current Displacement Transducer* accurate to 0.1 $\mu$m. In particular the flow rate is recovered as

$$Q = \frac{Pressure\,Intensifier\,Displacement}{\Delta t} Ap_p \qquad (1)$$

where: $Q$ is the flow rate [$m^3$/sec]; *Pressure Intensifier Displacement* [m]; $\Delta t$: time interval [sec]; $A_{Pp}$: cross-sectional area of pore pressure intensifier piston [$m^2$].

[14] After each change in Pp we wait for an hour or more to allow the fluid flow rate to reestablish a steady state constant magnitude. An example of our measurements is represented in Figure 3.

[15] In our system, (Figure 2b) the pore fluid pressure is the same at the top of the sample and at the center of the fracture (e.g., low transmissivity fracture relative to the borehole), while it is 0 at the fracture edge. Thus the values of Pp reported in Table 2 correspond also to the values of the pore fluid pressure gradient ($\Delta$Pp) applied across the fracture.

[16] Figure 3 shows the complete history of experiment p2117. Before locking the platen displacements to confine the sample, the axial stress reaches 8 MPa. Once the platens are locked the pore fluid pressure is successively incremented from a minimum of 0.2 MPa to a maximum of 2 MPa through intermediate levels of 0.5 MPa, 1 MPa and 1.5 MPa. Incidental changes in total axial stress are plotted together with the evolution of influent flow rate to the fracture (Figure 3).

[17] In particular, we correct for elastic effects of the loading frame using the recorded axial stress values after having compared the stiffness of the loading frame and

**Table 2.** Variables and Results[a]

| Westerly Granite $\phi$: 44 (mm) L: 100 (mm) | | | | | | | |
|---|---|---|---|---|---|---|---|
| | Experiment Variables | | Results | | | | |
| | $\sigma$ (MPa) | | $\sigma$ (MPa) | | Flow Rate ($m^3$/sec) | | |
| Test | Initial Value | Pp or $\Delta$Pp (MPa) | Peak Value | Residual Value | Peak Value | Residual Value | b ($\mu$m) |
| p1989 | 16 | 0.5 | 15.2 | 14.6 | 9.96e-9 | 2.32e-9 | 2.75 |
| | | 1 | 13.4 | 13.23 | 1.01e-8 | 2.45e-9 | 2.25 |
| | | 1.5 | 12.25 | 12.2 | 6.24e-9 | 5.25e-9 | 2.50 |
| P2114 | 8.6 | 0.5 | constant | | 9e-12 | 9e-12 | No Fracture |
| | | 1 | | | 1.05e-11 | 1e-11 | |
| | | 2 | | | 2e-11 | 1.05e-11 | |
| | | 4 | | | 3e-11 | 2e-11 | |
| | | 8 | | | 8e-11 | 5e-11 | |
| p2117 | 8 | 0.2 | 7.09 | 7.03 | 4.7e-8 | 2.3e-10 | 1.82 |
| | | 0.5 | 7.04 | 7 | 2e-8 | 4.5e-10 | 1.58 |
| | | 1 | 7.02 | 7.06 | 1.5e-8 | 7.9e-10 | 1.45 |
| | | 2 | 7.09 | 7.15 | 1.01e-8 | 7.9e-10 | 1.169 |
| p2398 | 8 | 0.2 | 6.6 | 6.96 | 1.88e-7 | 5.69e-9 | 2.05 |
| | | 0.5 | 6.97 | 6.94 | 3.48e-8 | 6.4e-10 | 1.69 |
| | | 1 | 7.9 | 8.12 | 1.28e-8 | 6.3e-10 | 1.43 |
| | | 1.5 | 8.7 | 9.2 | 1.10e-8 | 7.5e-10 | 1.33 |
| p2458 | 12 | 0.2 | 9.8 | 9.55 | 5.14e-8 | 3.1e-10 | 1.69 |
| | | 0.5 | 9.56 | 9.65 | 3.28e-8 | 4.0e-10 | 1.48 |
| | | 1 | 9.66 | 9.74 | 3.88e-9 | 9.4e-10 | 1.58 |
| | | 1.5 | 9.75 | 9.86 | 1.02e-8 | 2.91e-9 | 1.99 |
| | | 2 | 9.8 | 10.4 | 3.0e-9 | 8.2e-10 | 1.19 |
| p2531 | 8 | 1 | 6.6 | 6.96 | 3.45e-8 | 2.7e-10 | 2.05 |
| | | 1.5 | 6.97 | 7.02 | 9.22e-9 | 3.9e-9 | 1.69 |
| | | 2 | 7.9 | 8.2 | 2.87e-8 | 8.47e-9 | 1.43 |

[a] $\sigma$, total axial stress; Pp, pore fluid pressure; b, hydraulic aperture; $\Phi$, diameter; L, length.

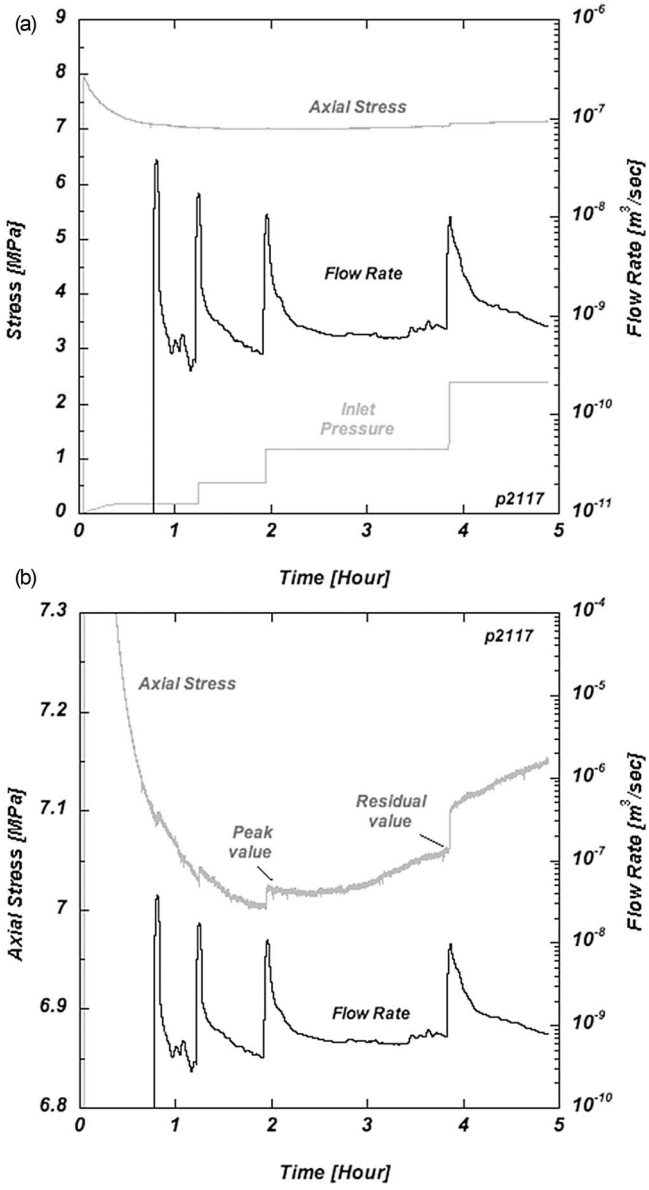


**Figure 3.** (a) Flow rate and applied axial stress evolution as a function of time at different values of inlet pressure and (b) details of the recorded changes of the axial stress (for details see Table 2).

platens (0.5 kN/$\mu$m) with the one of the sample which is $\sim$1 kN/$\mu$m.

## 3. Results

[18] Results from the experiments are highly reproducible. Correspondingly we show a representative example of the detailed time series for test p2117 (Figure 3) and augment this with derived parameters from the remaining full suite of experiments (Table 2). Key reported parameters are those for initial and ultimate flow rates and the total axial stress (*peak* and *residual*) corresponding to each applied increment of pore fluid pressure. More generally our principal laboratory data are the timing of the applied fluid pressurization and the history of outflow from the fracture (measured as the rate of inflow at the top of the sample).

[19] These experiments show that in a regime of zero axial displacement (the load point of the axial ram is stationary) and steady state flow, increments of pore fluid pressure cause both permanent variations of total normal stress and temporal changes of the flow rate in the fractures (Figure 3b). Once a pore fluid pressure increment is applied, in fact, the flow rate initially jumps to a high magnitude but then slowly drops to background magnitudes with time.

[20] We first associate the initial increase in flow rate with the dilation of the fracture driven by the undrained application of pore fluid pressure in the fracture. The second and subsequent slow reduction in flow rate toward the initial flow rate is associated with the compaction of the fracture driven by the expansion of the rock matrix surrounding the fracture. In particular the matrix expands in response to the drained infusion of fluid into the matrix, the corresponding increase in pore fluid pressure within that matrix and the resulting reduction in effective stresses as total axial stresses remain constant. This behavior is discussed and explored below (see Figure 3 and Table 2).

[21] In order to confirm that the observed peaks in flow rates (Figure 3) are not merely an increased flux associated with hydraulic storage, measurements of matrix storage have been conducted on an unfractured sample with a blind axial borehole (Figure 4). The experiment (p2114 on Table 2) confirms this hypothesis for the same values of pore fluid pressure applied to the fractured samples - the flow rates recorded during test p2114 are steady and about 2 orders of magnitude lower than those recorded for the fractured samples at steady flow rates conditions (for details see exp #: p2114 in Table 2 and Figure 4).

## 4. Data Analysis

[22] We analyze our experimental data using non-dimensional parameter groupings. In particular we plot both

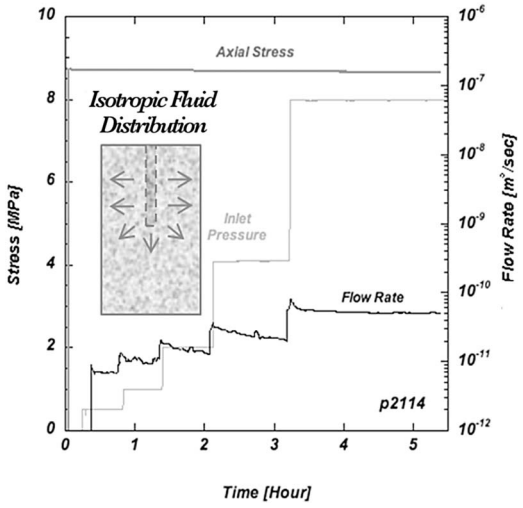


**Figure 4.** Evolution of flow rate and applied axial stress with time at different values of inlet fluid pressure for an intact sample of Westerly granite penetrated by a blind axial core hole.

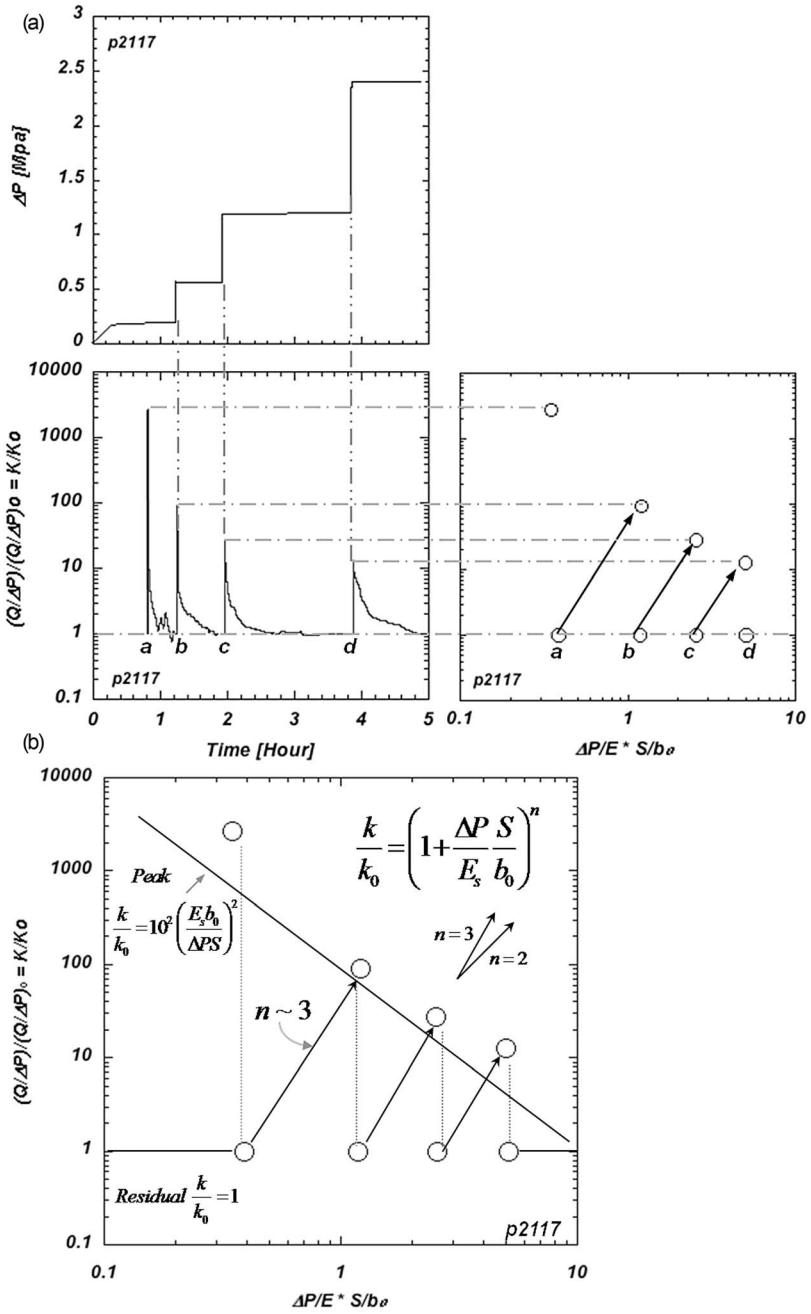


**Figure 5.** Plot of experiment P2117 showing residual and peak relative permeabilities when fluid pressure is raised in the fracture. Normalized permeability change (left axis) $(Q/\Delta P)/(Q/\Delta P)_0 = k/k_0$ is shown relative to the augmented pressure $\Delta P$ where the pressure is normalized by deformation modulus ($E$), fracture spacing ($S$) and initial fracture aperture ($b_0$). Arrows show the trajectory of the rise from residual permeability as pressure is augmented. Arrows show trajectories of equation (11) for values of the exponent, $n$. (a) Shown is the relation between the reduced experimental data of Figure 3 as the pressure is raised (top left) and the translation of these data to the form of Figure 5.

the peak and the residual flow rates recovered from the experiments as shown schematically in Figures 5 and 6. Data are shown in normalized form as recovered from experiments on fractured samples (for values see Table 2 and for a graphical example see inset of Figure 5) as normalized flow rates ($Q$): $(Q/\Delta P)/(Q/\Delta P)_0$, relative to normalized pore pressure magnitudes ($\Delta P$): $(\Delta P/E)^*(S/b_0)$ using deformation modulus ($E$), fracture spacing ($S$) and initial fracture aperture ($b_0$). These parameters are reciprocally related as will be demonstrated.

### 4.1. Permeability Augmentation and Relaxation

[23] We develop scaling laws to link changes in permeability to applied changes in effective stresses driven by augmentation of fluid pressures within the fracture. At two

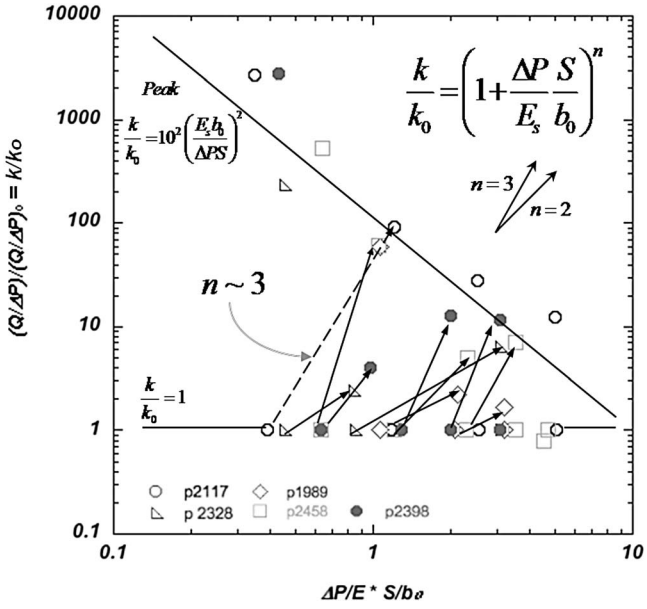


**Figure 6.** Trajectories of permeability change for the full ensemble suite of experiments. Arrows show adjacent points as fluid pressure is augmented from the prior steady magnitude with designated null permeability change (base of arrow) to the incremented fluid pressure (top of arrow. Arrows show trajectories of equation (11) for values of the exponent, $n$. All data shown as a function of normalized applied fluid pressure $\Delta P/E \times S/b_0$ (for details see Table 2 and the explanation in section 4.

different times $t_0$ and $t$, permeability may be defined as [e.g., *Ouyang and Elsworth*, 1993]

$$k_o = \frac{b_o^3}{12S} \sim \left(\frac{Q}{\Delta P}\right)_0 \tag{2}$$

$$k = \frac{(b_o + \Delta b)^3}{12S} \sim \frac{Q}{\Delta P} \tag{3}$$

where: $k_0$ and $k$ [$m^2$] are the permeabilities at times $t_0$ and $t$, where $b_o$ is the initial hydraulic aperture of the fracture and $\Delta b$ is the change in aperture at time $t$ [m]; $S$ is the spacing between two adjacent fractures (in our case $S$ is the length of the sample): [m], $Q$ is the flow rate: [$m^3$/sec] and $\Delta P$ is the inlet pore fluid pressure within the central borehole of the sample: [Pa].

[24] The ratio between $k$ and $k_0$ is

$$\frac{k}{k_o} = \left(1 + \frac{\Delta b}{b_0}\right)^3 \sim \frac{Q}{\Delta P} \Big/ \left(\frac{Q}{\Delta P}\right)_0 \tag{4}$$

enabling the applied and measured flow rates to be related directly as permeability changes, and ultimately linked to the anticipated changes in deformation across the fracture faces, $\Delta b$. We explore the possibility of linking permeability changes to deformation in the following.

### 4.2. Deformation Response to Pressure Augmentation

[25] The experimental geometry comprises locked platens with zero axial displacement (Figure 7) and containing a single fracture perpendicular to this loading axis of zero net strain. Thus zero axial strain is the particular condition of the experiment and represents the anticipated conditions of zero net volumetric strain *in situ*. We consider this serial geometry of matrix and embedded fracture [*Elsworth and Bai*, 1992; *Bai et al.*, 1999; *Chen and Bai*, 1998] with the matrix of length $S$ and containing a single fracture. With compressive stress and compactive deformation positive then the shortening across a fracture $\Delta u_f$ may be related to the effective stress, $\Delta\sigma'$, total stress, $\Delta\sigma$, and applied fluid pressure in the fracture, $\Delta p_s$, the Biot coefficient [*Biot and Willis*, 1957], $\alpha_s$, and stiffness of the fracture, as $K_n$ (Table 1)

$$\Delta u_f = \frac{\Delta\sigma'}{K_n} = \frac{\Delta\sigma - \alpha_f \Delta p_f}{K_n}. \tag{5}$$

[26] Similarly, for the solid matrix, the compression $\Delta u_s$ may be defined in terms of deformation modulus, $E_s$,

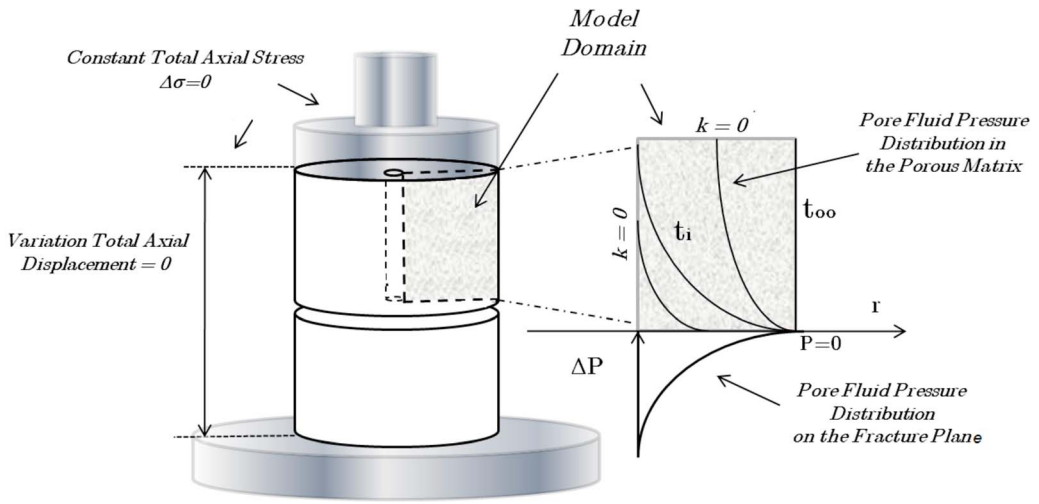


**Figure 7.** Schematic of the poromechanical mechanism responsible for the combined radial and longitudinal compaction of the sample and reciprocal closure of the fracture.

fracture spacing, $S$, Biot coefficient, $\alpha_s$ and fluid pressure in the solid $\Delta p_s$ as

$$\Delta u_s = \frac{S\Delta\sigma'}{E_s} = \frac{(\Delta\sigma - \alpha_s \Delta p_s)S}{E_s}. \quad (6)$$

[27] Since displacements of the core are restricted at the platens then $\Delta u_s + \Delta u_f = 0$ and we can consider either of two loading conditions applied to this arrangement. The first is the *undrained condition* where the fracture is pressurized and no pressure initially is developed in the solid matrix ($\Delta p_f > 0$; $\Delta p_s = 0$). The second is the *drained condition* where the pore fluid pressures in both fracture and matrix are ultimately identical ($\Delta p_f = \Delta p_s$). We follow this undrained condition. The peak pressure change that induces a dynamic increase in permeability is recovered by first defining the total stress induced by augmenting fluid pressure. Substituting the constitutive equations of (5) and (6) into $\Delta u_f + \Delta u_s = 0$ yields

$$\Delta\sigma\left(\frac{S}{E_s} + \frac{1}{K_n}\right) - \alpha_s \Delta p_s \frac{S}{E_s} - \alpha_f \Delta p_f \frac{1}{K_n} = 0. \quad (7)$$

[28] Where the induced pressure in the solid component, $\Delta p_s$ is null then the induced total stress is defined as

$$\Delta\sigma = \frac{\alpha_f \Delta p_f}{1 + K_n S/E_s} \quad (8)$$

[29] This total stress may be substituted into the displacement equation (6) as

$$\Delta u_s = -\Delta u_f = \frac{1}{1 + K_n S/E_s} \frac{S\alpha_f \Delta p_f}{E_s} \quad (9)$$

and finally the result recovered from the permeability relations (equation (4)) is

$$\frac{k}{k_o} = \left(1 + \frac{\alpha_f}{1 + K_n S/E_s} \cdot \frac{S\Delta P}{b_o E_s}\right)^3 \quad (10)$$

[30] Furthermore, for the typical case where the fracture is much softer than the surrounding matrix from which it is derived ($K_n S \leq E_s$) this yields the permeability equation used in the following as

$$\frac{k}{k_o} = \left(1 + \alpha_f \frac{S\Delta P}{b_o E_s}\right)^3 = \frac{Q}{\Delta P} \Big/ \left(\frac{Q}{\Delta P}\right)_0 \quad (11)$$

[31] We use this expression to define the principal quantities recovered from experiments. Within each experiment and for each incremented magnitude of pore fluid pressure, we compute $\frac{Q}{\Delta P}$ and $\left(\frac{Q}{\Delta P}\right)_0$ using respectively the peak and residual values of flow rates and their respective values of pore fluid pressure (Table 2). We then normalize the results relative to the smallest $\left(\frac{Q}{\Delta P}\right)_0$ calculated.

[32] To relate these results to the unmeasured magnitudes of effective stress within the core of Westerly granite we then use the "indirectly" determined effective stress $\frac{S\Delta P}{b_o E_s}$ where the initial aperture is recovered by substituting $k = \frac{b_o^2}{12}$ into an expression to determine transmissivity from the radial flow geometry as

$$T = \frac{\rho g k b_o}{\mu} = \frac{Q}{2\pi(h_2 - h_1)} \ln\frac{r_2}{r_1} \quad (12)$$

where the terms are: $T$: transmissivity of the fracture [m$^2$/sec] at steady radial flow [m$^2$/sec]; $\rho$: water density [kg/m$^3$]; $g$: gravitational acceleration [m/sec$^2$]; $k$: permeability at steady state [m$^2$]; $b_o$: hydraulic aperture [m]; $\mu$: dynamic viscosity [Pa sec]; $Q$: flow rate at steady state conditions [m$^3$/sec]; $r_1$ and $r_2$: are respectively radius of the injection conduit and of the exterior fracture contour at the core boundary [m]; and, $h_2 - h_1$: water head differential computed from the pore pressure gradient [m] (see Table 2).

[33] With storage effects confirmed negligible (Figure 4), the peak and residual flow rates are assumed to represent the influence of an undrained increase in fracture permeability (by pressure augmentation) that resets to background permeability as effective stresses in the matrix return to pre-injection magnitudes.

### 4.3. Axisymmetric Analysis

[34] In our system where overall strains are constrained, the injection of fluid into a fracture results in a single instantaneous change in total axial stress for both the fracture and adjacent matrix, as described above. In the case where the Biot-Willis coefficients for the fracture and matrix are assumed to be unity, the total stress change in the fracture is equal to the magnitude of the applied pore pressure and the consequent change of effective stress in the fracture is null [*Wang*, 1993].

[35] The observation that both the pre-pressurization and long-term permeabilities of the fracture are the same suggests that the Biot-Willis coefficient is close to unity for both fracture and matrix. Regardless of the assumption of unity for the Biot-Willis coefficient, we see that an increase in the applied fluid pressure instantly augments the total axial stress in the fracture and matrix. Since pore fluid pressures are slow to build in the matrix, the instant application of pore fluid pressures in the fracture results in an instant increase in effective axial stress within the matrix that shortens the matrix and dilates the fracture by compensation (even though the change in effective axial stress in the sample is constant). However, the effective axial stresses within the low permeability and rigid matrix reduce with time as pore fluid pressures grow with fluid transfer from the fracture (and the central injection hole) to the matrix.

[36] As a result, the matrix initially contracts upon the applied increase in pore fluid pressure in the fracture, the fracture dilates, and this dilation is recorded by the increased permeability of the fracture (Figure 5 inset). The slow diffusion of fluid into the matrix when total axial stresses remain constant results in a decrease in effective axial stress in the matrix, a dilation of the matrix and a corresponding re-compression of the fracture. The observation that permeability resets to its initial pre-pressure-augmented magnitude is a consequence of the total stress change being

driven by fluid pressure alone. In our experimental geometry, the changes in total stress are small (see Table 2 and Figure 3) since pore fluid pressures are predicted to fall logarithmically from the peak magnitude in the center of the fracture to zero (atmospheric) at the fracture periphery.

[37] A necessary condition for the mechanism we invoke to cause this observed permeability transient, is for a transient dynamic stress – or the resulting remnant static stress – to induce an undrained rapid increase in pore fluid pressure, possibly as a result of void compaction. This undrained change in pore pressure occurs for zero lateral strain and the initial increase in pore fluid pressure would dilate fractures set in a high-rigidity low-permeability matrix. With time, the excess pore fluid pressure in the fracture diffuses into the matrix, and the resulting reduction in effective axial stress forces the block to dilate and the fracture to sympathetically compact. At the completion of this process, the fracture returns to its original aperture and the permeability is reset to its original magnitude.

[38] In our experiments, the initial change in fracture aperture is driven by fluid pressure, as indicated by equation (9). This occurs immediately as the pressure rises. As a consequence, we record an instantaneous increase in the steady flow rate in response to this change in aperture and related permeability (Figure 5). Fluid storage within the fracture system and within the low-volume void system of the Westerly matrix is very small in comparison to the volumetric flow-through rate of the fracture (Figure 4), and hence, flow within the fracture system is always close to a steady state. Consequently these flow measurements are direct measurements of the deformation response of the fracture and changes in permeability manifest within the fracture.

[39] Figure 5 shows the transformation of raw time series data (p2217) for the change in flow rate and related permeability (Figure 5 inset) to the reduced non-dimensional parameters used in the main panel of Figure 5. The arrows show the trajectory of permeability increase as pressure is augmented. The direction of this permeability change is close to that anticipated form $k/k_0 = (1 + (S\Delta P/b_o E_s))^n$ with $n \sim 3$ as apparent in the Figure 5 and following from equation (11). Responses are also bounded between an upper limit for the peak response and a lower limit for residual response. This behavior is apparent for all experiments on multiple samples as shown in Figure 6. The general trends in permeability change generally follow $k/k_0 = (1 + (S\Delta P/b_o E_s))^3$ as apparent from the trajectories shown in Figure 6. The upper bound on the peak permeability change suggests that as pressure becomes larger, and effectives stresses smaller the effective change in permeability is correspondingly reduced. This may result from a constant change in solid shortening $\Delta b$ having progressively less influence on permeability change as the fracture dilates and $b_o$ becomes larger at lower absolute effective stresses. The peak change in permeability is observed to have an upper bound of $\frac{k}{k_o} = 10^2\left(\frac{b_o E_s}{S\Delta P}\right)$ and a lower bound of $\frac{k}{k_o} \sim 1$.

[40] The rate at which permeability recovers to the background magnitude is indexed by the rate of pressure-diffusion of the incremented pore pressure within the central conduit and fracture to reach a new steady pressure distribution. This is controlled by the radial and longitudinal diffusion of pore fluids into the matrix and the accompanying poroelastic deformation of the rock matrix. The pore fluid pressure diffuses according to the relation

$$cv\left(\frac{1}{r}\frac{\partial P}{\partial r} + \frac{\partial^2 P}{\partial r^2} + \frac{\partial^2 P}{\partial z^2}\right) = \frac{\partial P}{\partial t} \tag{13}$$

where the hydraulic diffusivity $cv$ [$m^2$/sec] is defined in terms of the bulk modulus of the matrix $E_b$ as

$$cv \sim \frac{k}{\mu} E_b \tag{14}$$

[41] We consider geometry where the upper boundary of the sample is fixed and pore fluid pressures are augmented in the center of the fracture and vary logarithmically in the radial direction along this boundary according to the equation (13). As a consequence of this pore fluid pressure-diffusion into the matrix, effective axial stresses are reduced and the matrix of the Westerly granite dilates against the stiffness of the resisting fracture (Figure 7). The resulting differential deformation of the fracture is recorded as a permeability change apparent in the change in fracture inflow rate. Rates of change of aperture are conditioned by a diffusive time and are constant for all magnitudes of pore fluid pressure change. However, larger changes in pressure will yield larger changes in effective axial stresses and correspondingly larger absolute changes in permeability – although rates of recovery of normalized permeability will be sensibly identical for magnitudes of pressure increments.

[42] The results of this computation are shown in Figure 8 using the data collected from experiment p2117. These data cover the entire spectrum of responses represented in Figure 6. These results may be compared with evaluations for the average rates of deformation of the fracture and using mean pressure changes within the sample. This progress to equilibration may be indexed by the average degree of equilibration $Um$ from the solution where the true logarithmic distribution of basal pressure is used. The degree of equilibration $Um$ varies from 0 to 1 and is conditioned by a diffusive time, $Tv$. The theoretical values have been computed by a two dimensional FEMlab model computing the solution of equation (13) for the same boundary conditions represented in Figure 7 and described above. Experimental magnitudes are evaluated from

$$Um = \frac{S(t)}{Sf} \tag{15}$$

where $S(t)$ is the displacement at time $t$ and $Sf$ is the displacement at time infinity when the system is fully equilibrated.

[43] In our experiments the displacements ($S(t)$) correspond to scaled changes in aperture of the fracture and are conditioned by the stiffness of the matrix of the Westerly granite and the stiffness of the fracture. Each transient change of flow rate recorded during experiment p2117 has been separately considered and the corresponding values of the hydraulic aperture of the fracture determined from the measured flow rate and calculated permeability. These are determined for the full history of flow rates using equation (12). The theoretical and experimental normalized magnitudes of fracture closure/opening are reported on a

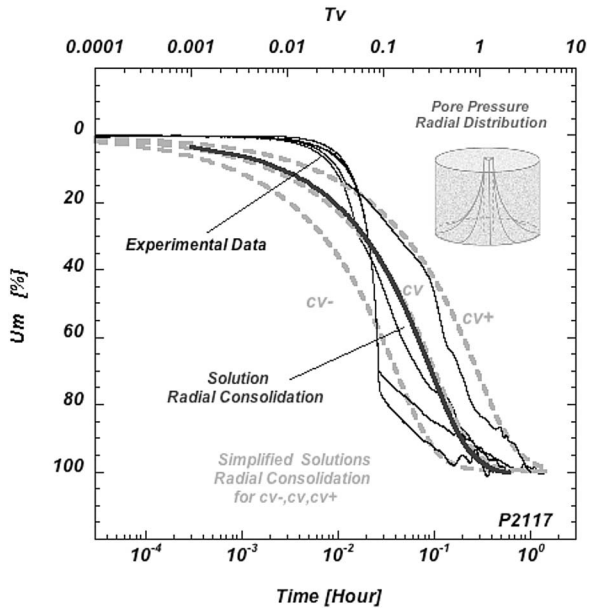


**Figure 8.** Comparison between the predicted rates of matrix dilation and fracture re-compaction (*Um*) relative to dimensionless time *Tv* (line: *Solution Radial Consolidation*) and the experimental response relative to real time (lines: *Experimental Data*). The bounding gray lines represent results for bounding magnitudes of the hydraulic diffusivity *cv* of respectively: *cv*−: 1.46 *$10^{-6}$ [$m^2$/sec]; *cv*: 5.86*$10^{-7}$ [$m^2$/sec]; *cv*+: 2.1*$10^{-7}$ [$m^2$/sec].

common scale in Figure 8 as a function of diffusive time constant *Tv*. The analytical magnitudes are recovered as [*Sivaram and Swamee*, 1977]

$$Um = \frac{\left(4\frac{Tv}{\pi}\right)^{0.5}}{\left[1+\left(4\frac{Tv}{\pi}\right)^{2.8}\right]^{0.179}} \tag{16}$$

where *Tv* at any time ***t*** is given by

$$Tv = \frac{cv \cdot t}{R^2} \tag{17}$$

where *cv* is hydraulic diffusivity [$m^2$/sec], *R* is the length of the sample synonymous with S [m], and *t* is the real time [sec]. The experimental data may be fit around the time to 50% equilibration. Matching the experimental data to the theoretical magnitudes yields a predicted hydraulic diffusivity for the sample of *cv*: 5.86*$10^{-7}$ [$m^2$/sec] and is bounded by magnitudes half an order of magnitude offset in time as *cv*−: 1.46*$10^{-6}$ [$m^2$/sec]; *cv*+: 2.1*$10^{-7}$ [$m^2$/sec] (see Figure 8).

[44] We compare these magnitudes with independent measurements of transport parameters recovered from steady flow experiments and from the deformation modulus of the rock. In particular the value of permeability (*k*) measured on an intact sample of Westerly granite (at an axial stress of 10 MPa) is 7*$10^{-19}$ [$m^2$]. Thus the hydraulic diffusivity defined as $cv = \frac{k}{\mu}E_b$ (see equation (14)) is recovered as 1.57*$10^{-8}$ [$m^2$/sec] and is consistent with that recovered from the curve fit: *cv*: 2.45*$10^{-7}$ [$m^2$/sec].

[45] For each value of *cv* we compute respectively the values of T*v* corresponding to the real times (from equation (17)), and then the corresponding values of the average level of compaction (from equation (16)). The evolution of the average magnitude of fracture compaction (or equivalent matrix dilation) as a function of real time is reported in Figure 8. As Figure 8 shows, the experimental values are consistently matched by the analytical results, suggesting that radial and longitudinal dilation conditioned by pore fluid pressure diffusion is the dominant mechanism controlling the dynamics of the experiment. This conclusion is reinforced as we compare the analytical values of flow rate with the experimental observations.

[46] From the theoretical values of the average magnitude of compaction, in fact, rearranging equation (15) and substituting *Sf* with the last experimental value of aperture of the fracture we compute the corresponding values of hydraulic aperture of the fracture. These are then substituted into equation (12) in order to recover the corresponding values of flow rate. These are reported in Figure 9 illustrating that the analytical and experimental values are in good agreement.

## 5. Conclusions

[47] Our experiments explore potential causal mechanism for transient changes in permeability that may play an important role in Earth's crust. We document variations of permeability in fractured rocks where strains (perpendicular to the plane of fracture) are constrained and where the only forcing mechanism is a step change in applied pore fluid pressure. This stimulus is shown to induce a transient variation in the permeability of the fracture as the fracture initially dilates and then compacts as pore fluid diffusion into

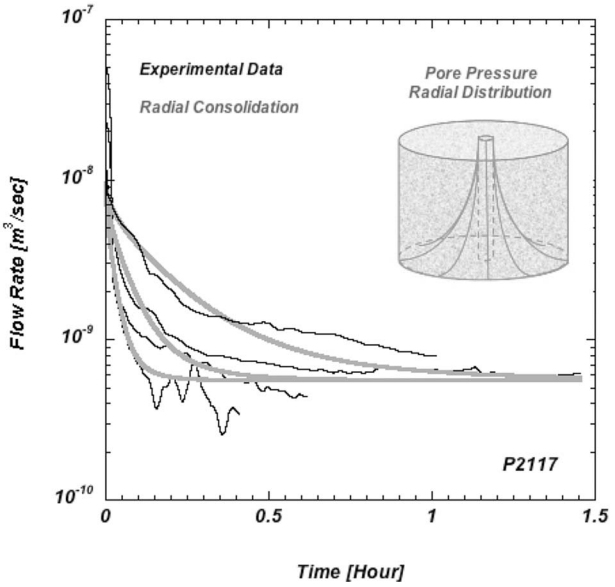


**Figure 9.** Comparison between modeled and experimental magnitudes of the decay in radial flow rate with time.

the surrounding matrix reverses and resets the deformation of the fracture. This mechanism is a consequence of the partitioning of the effective stress between the fracture (that responds quickly to the perturbation) and the matrix that responds slowly. We have identified two principal mechanisms for this response. The first is shortening of the matrix surrounding the fracture under undrained loading when permeability within the fracture concomitantly increases. The second is the slow expansion of the matrix as pore fluid pressures diffuse in thereby reducing fracture permeability in the adjacent fracture. These behaviors are capable of replicating the observed response of the fracture as a pulse pressure change is applied to the sample. The initial augmentation of permeability is rapid and is controlled by the time-scale of pressurization. The recovery to background permeability is a slower transient and scales inversely with permeability and proportionally to the square of fracture spacing (drainage path length). Thus permeability recovery times of the order of an hour (Figure 9) measured on centimeter-sized samples in the laboratory scale to recovery times of $10^4$ hours (420 days) on meter-spaced fractures, congruent with field observations.

[48] **Acknowledgments.** This work is the result of partial support from the U.S. Department of Energy under project DOE-DE-FG36-04GO14289 and from the National Science Foundation under projects EAR-0510182, CMMI-0927266, EAR054570, EAR0746192, and OCE-0648331. This support is gratefully acknowledged. We thank Yves Bernabe and one anonymous reviewer for comments that improved the manuscript.

## References

Bai, M., F. Ming, D. Elsworth, and J. C. Roegiers (1999), Analysis of stress-dependent permeability in nonorthogonal flow and deformation fields, *Rock Mech. Rock Eng.*, *32*, 195–219, doi:10.1007/s006030050032.

Biot, M. A., and D. G. Willis (1957), The elastic coefficients of the theory of consolidation, *J. Appl. Mech.*, *24*, 594–601.

Chen, M., and M. Bai (1998), Modeling stress-dependent permeability for anisotropic fractured rocks, *Int. J. Rock Mech. Min. Sci.*, *35*, 1113–1119, doi:10.1016/S0148-9062(98)00167-3.

Connolly, J. A. D. (1997), Devolatilization-generated fluid pressure and deformation-propagated fluid flow during prograde regional metamorphism, *J. Geophys. Res.*, *102*, 18,149–18,173, doi:10.1029/97JB00731.

Connolly, J. A. D., and A. B. Thompson (1989), Fluid and enthalpy production during regional metamorphism, *Contrib. Mineral. Petrol.*, *102*, 347–366, doi:10.1007/BF00373728.

Dutrow, B., and D. Norton (1995), Evolution of fluid pressure and fracture propagation during contact metamorphism, *J. Metamorph. Geol.*, *13*, 677–686, doi:10.1111/j.1525-1314.1995.tb00251.x.

Elkhoury, J. E., E. E. Brodsky, and D. C. Agnew (2006), Seismic waves increase permeability, *Nature*, *441*, 1135–1138, doi:10.1038/nature04798.

Elsworth, D., and M. Bai (1992), Flow-deformation response of dual porosity media, *J. Geotech. Geoenviron. Eng.*, *118*, 107–124.

King, C.-Y., S. Azuma, G. Igarashi, M. Ohno, H. Saito, and H. Wakita (1999), Earthquake related water-level changes at 16 closely clustered wells in Tono, central Japan, *J. Geophys. Res.*, *104*, 13,073–13,082, doi:10.1029/1999JB900080.

Lowell, R. P., P. Van Cappellen, and L. N. Germanovich (1993), Silica precipitation in fractures and the evolution of permeability in hydrothermal upflow zones, *Science*, *260*, 192–194, doi:10.1126/science.260.5105.192.

Lowell, R. P., P. A. Rona, and R. P. Von Herzen (1995), Seafloor hydrothermal systems, *J. Geophys. Res.*, *100*, 327–352, doi:10.1029/94JB02222.

Manga, M., and E. E. Brodsky (2006), Seismic triggering of eruptions in the far field: Volcanoes and geysers, *Annu. Rev. Earth Planet. Sci.*, *34*, 263–291, doi:10.1146/annurev.earth.34.031405.125125.

Manga, M., E. E. Brodsky, and M. Boone (2003), Response of stream flow to multiple earthquakes, *Geophys. Res. Lett.*, *30*(5), 1214, doi:10.1029/2002GL016618.

Muir-Wood, R., and G. King (1993), Hydrological signatures of earthquake strain, *J. Geophys. Res.*, *98*, 22,035–22,068, doi:10.1029/93JB02219.

Nur, A., and J. Walder (1990), Time-dependent permeability of the Earth's crust, in *The Role of Fluids in Crustal Processes*, edited by J. D. Bredehoeft and D. Norton, pp. 113–127, Natl. Acad. Press, Washington, D. C.

Ouyang, Z., and D. Elsworth (1993), Evaluation of groundwater flow into mined panels, *Int. J. Mech. Min. Sci. Geomech. Abstr.*, *30*(2), 71–79, doi:10.1016/0148-9062(93)90701-E.

Quilty, E., and E. A. Roeloffs (1997), Water level changes in response to the December 20, 1994 M4.7 earthquake near Parkfield, California, *Bull. Seismol. Soc. Am.*, *87*, 310–317.

Rice, J. R. (1992), Fault stress states, pore pressure distributions, and the weakness of the San Andreas Fault, in *Fault Mechanics and Transport Properties of Rocks*, edited by B. Evans and T. F. Wong, pp. 475–503, Academic, London, doi:10.1016/S0074-6142(08)62835-1.

Roeloffs, E. (1996), Poroelastic methods in the study of earthquake related hydrologic phenomena, in *Advances in Geophysics*, vol. 37, edited by R. Dmowska, pp. 135–195, Academic, San Diego, Calif.

Roeloffs, E. A., S. S. Burford, F. S. Riley, and A. W. Records (1989), Hydrologic effects on water level changes associated with episodic fault creep near Parkfield, California, *J. Geophys. Res.*, *94*, 12,387–12,402, doi:10.1029/JB094iB09p12387.

Roelofts, E. A. (1998), Persistent water level changes in a well near Parkfield, California, due to local and distant earthquake, *J. Geophys. Res.*, *103*, 869–889, doi:10.1029/97JB02335.

Rojstaczer, S., and S. Wolf (1992), Permeability changes associated with large earthquakes: An example from Loma Prieta, California.10/17/89 earthquake, *Geology*, *20*, 211–214, doi:10.1130/0091-7613(1992)020<0211:PCAWLE>2.3.CO;2.

Rojstaczer, S., S. Wolf, and R. Michel (1995), Permeability enhancement in the shallow crust as a cause of earthquake-induced hydrological changes, *Nature*, *373*, 237–239, doi:10.1038/373237a0.

Sanford, W. E., and L. F. Konikow (1989), Simulation of calcite dissolution and porosity changes in salt water mixing zones in coastal aquifers, *Water Resour. Res.*, *25*, 655–667, doi:10.1029/WR025i004p00655.

Sivaram, B., and P. Swamee (1977), A computational method for consolidation coefficient, *Soil Found.*, *17*, 48–52, doi:10.3208/sandf1972.17.2_48.

Walder, J., and A. Nur (1984), Porosity reduction and crustal pore pressure development, *J. Geophys. Res.*, *89*, 11,539–11,548, doi:10.1029/JB089iB13p11539.

Wang, H. F. (1993), Quasi-static poroelastic parameters in rock and their geophysical applications, *Pure Appl. Geophys.*, *141*, 269–286, doi:10.1007/BF00998332.

D. Elsworth and I. Faoro, Department of Energy and Mineral Engineering, Center for Geomechanics, Geofluids, and Geohazards, EMS Energy Institute, Pennsylvania State University, 231 Hosler Bldg., University Park, PA 16802, USA. (igor.faoro@durham.ac.uk)

C. Marone, Department of Geosciences, Center for Geomechanics, Geofluids, and Geohazards, EMS Energy Institute, Pennsylvania State University, 536 Deike Bldg., University Park, PA 16802, USA.